Guided waves-based damage identification in plates through an inverse Bayesian process

W. Wu [a],[*], M.K. Malik [a],[c],[*], S. Cantero-Chinchilla [f], T. Lawrie [b], W.J. Yan [d], G. Tanner [b], R. Remenyte-Prescott [e], D. Chronopoulos [g]

[a] Institute for Aerospace Technology & The Composites Group, The University of Nottingham, NG7 2RD, United Kingdom
[b] School of Mathematical Sciences, University of Nottingham, NG7 2RD, United Kingdom
[c] Aernnova Engineering Division S.A., Madrid, 28034, Spain
[d] State Key Laboratory of Internet of Things for Smart City and Department of Civil and Environmental Engineering, University of Macau, China
[e] Resilience Engineering Research Group, Faculty of Engineering, University of Nottingham, University Park, Nottingham, NG7 2RD, United Kingdom
[f] Department of Mechanical Engineering, University of Bristol, Bristol, BS8 1TR, UK
[g] KU Leuven, Department of Mechanical Engineering & Mecha(tro)nic System Dynamics (LMSD), 9000, Belgium

ARTICLE INFO

ABSTRACT

The use of guided waves to identify damage has become a popular method due to its robustness and fast execution, as well as the advantage of being able to inspect large areas and detect minor structural defects. When a travelling wave on a plate interacts with a defect, it generates a scattered field that will depend on the defects geometry. By analysing the scattered field, one can thus characterize the type and size of the plate damage. A Bayesian framework based on a guided waves interaction model for damage identification of infinite plate for the first time is presented here. A semi-analytical approach based on the lowest order plate theories is adopted to obtain the scattering features for damage geometries with circular symmetry, resulting in an efficient inversion procedure. Subsequently, ultrasound experiments are performed on a large aluminium plate with a circular indentation to generate wave reflection and transmission coefficients. With the aid of signal processing techniques, the effectiveness and efficiency of the proposed approach are verified. A full finite element model is used to test the damage identification scheme. Finally, the scattering coefficients are reconstructed, reliably matching the experimental results. The framework supports digital twin technology of structural health monitoring.

1. Introduction

Plate like structures are widely applied in a range of systems including wind turbines, aircrafts, and ships. After the initial damage occurs, factors such as fatigue load will cause the damage to accumulate, which may lead to catastrophic failure of the entire system. Therefore, early damage detection is crucial for safety critical components of a structure. A step further is to characterize the damage by identifying its parameters such as the length and depth of a crack. In the context of structural health monitoring (SHM), online detection and characterization leads to a condition-based maintenance approach where the reliability of the structure can be quantified and maintenance procedures only performed when necessary. This is a cost-effective method of operation but requires reliable monitoring and inference techniques which can provide accurate parameters of the damage.

There are numerous established techniques for SHM [1–3]; ultrasonic guided waves are one such technique suitable for damage

detection and identification in thin plate like structures [4–6]. They are guided by the traction free surfaces of the structure and are able to travel large distances with relatively little attenuation. Moreover, they interact with any inhomogeneity in the structure and generate scattering waves. These scattering waves are unique to the type of damage and can be used to identify and characterize the shape of the damage. There are two main numerical approaches to damage identification using the signature of the damage: the data-based approach and the model-based approach [7,8]. The former is based on machine learning and advanced pattern recognition algorithm to identify the damage, which is built entirely upon modelling and/or experimental data [9–12]. Seventekidis et al. [9] updated finite element model based only on an initial experimental cost, then generated all data through the finite element calculated responses. Next, the data derived from the optimal FE model is able to train an accurate Deep Learning Convolutional Neural Network classifier that can predict adequately the

---

Nomenclature

$\mathscr{J}(\boldsymbol{\lambda}, \mathscr{D})$	the goodness-of-fit function
α_{ij}, β_{ij}	the matrix elements
$\mathbf{e}$	the error terms of the scattering coefficients
$\mathbf{s}_{\mathscr{D}}$	the scattering coefficients from the experiments
$\mathbf{s}_{\mathscr{M}}(\boldsymbol{\lambda})$	the scattering coefficients from the physical model
$\mathscr{D}$	the available data (i.e. the scattering coefficients)
$\mathscr{M}$	the model class
ω	frequency
ϕ, ψ	the scalar potential function
$\boldsymbol{\lambda}$	the damage characterization parameters
ρ	Density
Σ_e	the covariance matrix
σ_e	standard deviation
$\sigma_{rr}, \sigma_{r\theta}$	the stress components
υ	Poisson's ratio
a	the radius of partly through-thickness hole
$a_m - h_m$	the unknown expansion coefficients
b	the half thickness of the plate below the hole
c_1	the wave velocity of the $S0$
c_T	the wave velocity of the shear mode
E	Elastic stiffness
h	the half thickness of the plate
H_m	the Hankel function of the first kind
I_m	the modified Bessel function of the second kind
J_m	the Bessel functions of the first kind
k_1	the wavenumber of the $S0$
k_2	the wavenumber dependent on the plate thickness
K_m	the modified Bessel function of the second kind
k_T	the wavenumber of the shear mode
L_x, L_y	the dimensions of plate
$M_{rr}, M_{r\theta}$	the moments
$N_{rr}, N_{r\theta}$	the forces
u_r, u_θ, w	the displacement components
V_r	the generalized Kirchhoff stress

experimental benchmark states. Deraemaeker et al. [10] extracted two types of features from ambient vibration data to do damage detection; factor analysis is used to consider the environmental factors. There are also many experimental approaches for damage detection using guided waves but they are not the focus of this research [13]. However, due to practical limitations, data acquisition from actual expected damage is still a great challenge. Therefore, model-based approaches are increasingly attracting attention.

The use of efficient physics-based models embedded in a statistical inference framework is popular where the experimentally derived damage features are directly used to solve an inverse problem to characterize the damage. Numerous researchers employed Bayesian inference for wave propagation-based damage detection [14–17]. Huang [18] summarized the fundamental principles of Bayesian analysis and computation and reviewed recent state-of-the-art practices of Bayesian inference in system identification and damage assessment for civil infrastructure. A multilevel Bayesian framework was presented to do the localization and identification based on a transient wave propagation model without any baseline comparison [19]. The method used complete time-domain ultrasound signals directly, which could reduce additional uncertainty; the influence of measurement noise was also considered, but real experiment data were not involved [19]. However, Bayesian inference approaches are faced considerable challenges regarding computation time. Chiachio [20] presented a new approximate Bayesian computation technique (ABC), which can alleviate the computational cost of repeated physical model runs via bypassing the expensive evaluation of the likelihood function. Yan [21] constructed a Bayesian inference framework for damage identification in composite beam structures based on the hybrid wave finite element method; a cheap and fast Kriging surrogate model [22,23] was used to generate a database in advance, which can avoid using the physical model in the inverse procedure, thus enhancing the efficiency of the presented approach. However, the surrogate model will inevitably introduce errors into the calculation results and increase the uncertainty of the physical model.

For the inversion technique described above, the calculation of the scattered wavefield is required, which is similar to the tomographic technique. Using the scattering properties of Lamb waves, that is, the relationship between thickness variation and wave velocity, guided wave tomography reconstructs wave velocity from ultrasound measurements, and then reconstructs thickness from the reconstructed wave velocity [24]. Huthwaite [25] improved the accuracy of reconstructions of the small, high contrast defects expected from corrosion by using an iterating Hybrid Algorithm for Robust Breast Ultrasound Tomography. Rao et al. [26] developed a guided-wave tomography method based on full-waveform inversion (FWI) of isotropic plates; the finite difference method was used to solve the full-wave equation in frequency domain, and higher-order effects were considered. FWI was investigated further on the reconstruction accuracy of guided wave tomography in [27]. However, compared to probabilistic inverse problems, guided wave tomography is unable to account for modelling and experimental uncertainties.

Wave damage interaction models serve as the foundation of the Bayesian inference framework for damage characterization in ultrasonic measurements. They are not only expected to pull Bayesian inversion out of the time-consuming quagmire, but are also the key to improving the accuracy of inversion procedures. Soleimanpour [28] proposed a three-dimensional finite element model to predict the propagation of nonlinear Lamb waves induced by delamination in composite laminates. A generic finite element based computational scheme is presented for quantifying frequency-dependent interaction effects of guided waves with localized structural nonlinearities within complex composite structures [29]. Wilcox [30] described wave damage interaction based on a finite element model by constructing the scattering coefficient matrix, the S-matrix. This matrix describes the far-field scattered amplitudes as a function of the incident and scattered angle, the frequency and the incident and scattered mode as well as mode conversion. The S-matrix thus completely characterizes the scattering characteristics of ultrasonic waves at defects [31,32]. Malik [33] proposed a wave finite element based approach for complete transient simulation of ultrasonic guided waves in one-dimensional wave guides. A model reduction strategy is adopted to select the wave propagation mode based on the energy conservation of the finite size defects in the structure, thereby reducing the calculation time. However, numerical methods usually bring a huge computational burden which increases with frequency. They have thus severe limits in modelling guided wave scattering and defect interaction mechanisms especially in fully two or three dimensional simulations [34]. Analytical or semi-analytical methods can reduce the computational burden, and are thus good candidates for serving as a physical model in the inversion procedure. The interaction of guided waves with damage is a complex problem

where analytical models only exist for simple, regular damage geometries [35–39]. They are derived by normal-mode expansion and boundary condition matching. Scattering of guided waves by through-thickness and flat-bottomed cavities with irregular shapes were studied in [38,39]. Scattering of guided waves from part-depth circular holes was presented in [40]. Here, two different models are used to model the scattering phenomena, that is, a lower order plate theory and a 3D elasticity model. The lower order plate theory model is valid only in the low frequency regime but computationally efficient. The 3D elasticity model is more generally applicable but computationally intensive. A similar low-frequency scattering model for a through-thickness hole for the fundamental $S0$ mode was presented in [41]. Generally speaking, the numerical model is versatile, but the calculation takes a long time. Analytical or semi-analytical models have high computational efficiency, but are restricted to simple geometries or rely on approximations. Therefore, it is very important to choose an appropriate physical model that can not only have high computational efficiency, but also provide reliable damage characterization features for probabilistic models.

To address the above-mentioned critical issues, we develop and present for the first time a dedicated physics-based Bayesian framework for extracting damage characteristics from ultrasound measurements in plate like structures. A semi-analytical forward model is employed to perform rapid computations on wave/damage interactions including wave reflection, transmission and conversion which provides key elements for damage characterization. The presented approach is based on a combination of the Kirchhoff plate theory for flexural motion and the elementary Poisson theory for extensional motion under the assumption of spherical problem. The presented wave interaction damage model investigates the scattering of the lowest order symmetric Lamb mode from a circular hole of varying depth in a plate, and is used to efficiently generate the scattering coefficients corresponding to different defect parameters in the inversion process. By making full use of efficient semi-analytical model, a fast inversion framework is achieved. The likelihood function of Bayesian inference is formulated efficiently based on scattering contour in the frequency domain derived from the physical model directly, which can choose the excitation frequency reasonably and eliminate the influence of noise spectrum information on the inversion results. Implemented damage is identified within satisfactory confidence intervals for the experimental as well as the numerical case studies. The signal processing technique to extract scattering coefficients from ultrasonic measurements is provided in detail. The reflection coefficients of the lowest order symmetric Lamb mode are obtained from the raw ultrasound signals. The framework is also verified with numerical examples in different damage configurations. In general, the proposed Bayesian inversion is able to identify both the depth and the radius of a circular notch within the plate like structures using our fast wave scattering simulation scheme, while accounting for the modelling uncertainties and measurement errors in the inversion process.

The paper is organized as follows: the semi-analytical model for damage interaction simulation based on guided wave scattering properties is presented in Section 2. A signal processing technique is presented to obtain scattering coefficients in Section 3. The Bayesian inference framework for damage identification is introduced in Section 4. Section 5 provides a numerical example and an experimental case-study to illustrate the efficiency of the proposed methodology. Finally, concluding remarks are provided in Section 6.

2. Wave damage interaction model

Ultrasonic guided waves have the ability to travel across a structure and interact with damage. This interaction causes scattered waves that strongly depend on the geometric characteristics of the defect. The scattered field can be used to fully characterize the defect. In order to create a reliable damage identification framework, thousands of

computations are needed to generate a database containing measured structural responses. This makes the inversion procedure computationally expensive [9,21]. Yan [21] introduced an ultrafast hybrid wave finite element scheme, which was trained by a cheap and fast Kriging surrogate model to overcome the computational challenges. However, the surrogate model will inevitably introduce errors into the calculated results and increase the uncertainty of the physical model. Here, we present a semi-analytical approach fully using the symmetries in the problem to compute the scattering filed of the lowest order symmetric Lamb mode from a circular notch penetrating a plate. The model used in this paper is based on previous work by Grahn [40] wherein the scattering profile of a partially through-thickness hole is analysed. The methodology is presented in this section, and all the key equations are given.

Consider a homogeneous, isotropic, linearly elastic plate of thickness $2h$, spanning the infinite domain in x and y. With standard material properties E, ρ and v. At the origin is a hole of depth $2(h-b)$ and radius a, as illustrated in Fig. 1. We consider a plane $S0$ wave incident on the hole and determine the scattered field. Due to the asymmetry of the plate in the thickness direction, theories of extensional and flexural motion need to be combined to solve for the scattered field. For the extensional motion we use Poisson theory and for the flexural motion, Kirchhoff theory. These theories make the model reliable only in the low frequency regime, but remain valid for our purposes. Low frequency domain is defined on the plate as the wavelength divided by the thickness of the plate. In this study, the wavelength is much greater than the thickness of the plate, so the presented approach is valuable. More specifically, the upper limit of the low frequency regime depends on the thicknesses of plates and material properties, the frequency-thickness (fh) product. Higher-order modes are not excited below the cutoff fh product [42,43]. Wave finite element [33] or dispersion calculator [44] can be used to calculate the cutoff frequency. Based on these theories, the methodology is set up using the following 4 steps. (1) We begin by defining the scalar potentials across the entire plate for a given frequency, as well as the vertical displacement of the plate. (2) We use the defined scalar potential to determine the in-plane displacement field both inside and outside the hole. (3) With the plate displacements determined, the stresses and thus the resulting forces and moments across the plate can be found. (4) Once these quantities are determined, the boundary conditions at the hole edge are enforced allowing for the scattering profile to be determined. Below, these 4 steps are described in more detail giving an explicit recipe for their implementation.

(1) Consider the two scalar potentials ϕ and ψ for a given frequency that satisfy Helmholtz equation:

$$\nabla^2 \phi + k_1^2 \phi = 0, \quad \text{where} \quad k_1^2 = \frac{\omega^2}{c_1^2}, \quad c_1^2 = \frac{E}{\rho(1-v^2)},$$

$$\nabla^2 \psi + k_T^2 \psi = 0, \quad \text{where} \quad k_T^2 = \frac{\omega^2}{c_T^2}, \quad c_T^2 = \frac{E}{2\rho(1-v^2)}. \tag{1}$$

Where c_1 and c_T represent the wave velocity of the S0 and shear mode respectively. Assuming the plate is thin, or the frequency low, the vertical displacement component w is governed by:

$$\nabla^4 w - k_2^4 w = 0, \quad \text{where} \quad k_2^4 = \frac{2\rho h \omega^2}{D}, \quad D = \frac{8Eh^3}{12(1-v^2)}. \tag{2}$$

With the above equations in mind, consider the incident S0 wave as having potential defined as a linear superposition of Bessel functions of the first kind (J_m), expressed in cylindrical coordinates (r, θ).

$$\phi^{inc}(r, \theta) = h \sum_{m=-\infty}^{\infty} i^m J_m(k_1 r) e^{im\theta}. \tag{3}$$

Here, h is the half plate thickness and normalizes the function. Due to the different plate thicknesses the fields need to be split into inside
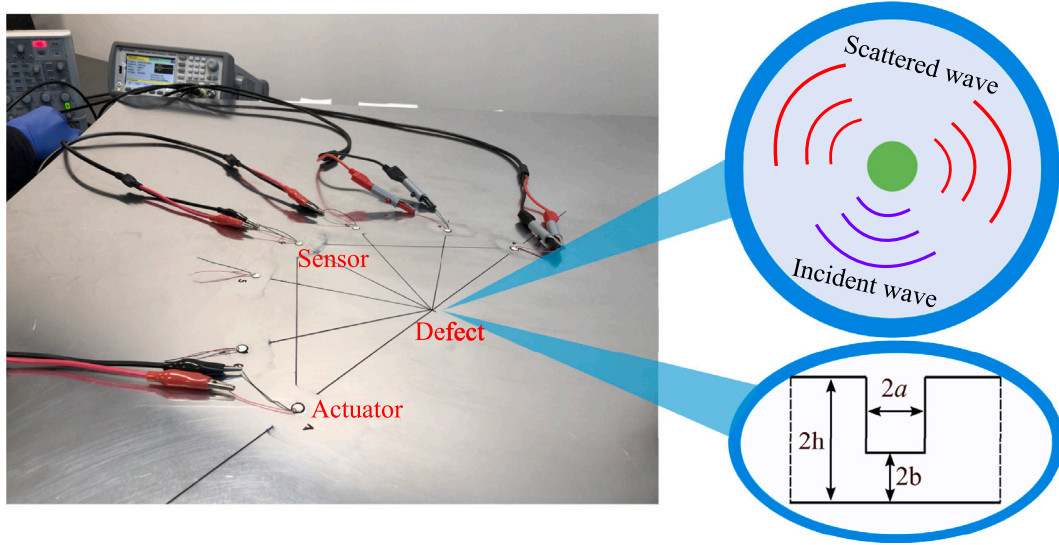
Fig. 1. Ultrasonic guided waves propagation and interaction scheme.

and outside the hole. The solutions outside the hole ($r > a$) are

$$\phi^>(r,\theta) = h \sum_{m=-\infty}^{\infty} a_m H_m(k_1 r)e^{im\theta}, \quad \psi^>(r,\theta) = h \sum_{m=-\infty}^{\infty} b_m H_m(k_T r)e^{im\theta},$$

$$\omega^>(r,\theta) = h \sum_{m=-\infty}^{\infty} \left\{ c_m H_m(k_2^h r) + d_m K_m(k_2^h r) \right\} e^{im\theta},$$

(4)

where H_m is the Hankel function of the first kind and K_m is the modified Bessel function of the second kind. Note the superscript on k_2^h which indicated the plate thickness outside the hole. The solutions inside the hole ($r < a$) can be written in the form

$$\phi^<(r,\theta) = h \sum_{m=-\infty}^{\infty} e_m J_m(k_1 r)e^{im\theta}, \quad \psi^<(r,\theta) = h \sum_{m=-\infty}^{\infty} f_m j_m(k_T r)e^{im\theta},$$

$$\omega^<(r,\theta) = h \sum_{m=-\infty}^{\infty} \left\{ g_m J_m(k_2^b r) + h_m I_m(k_2^b r) \right\} e^{im\theta},$$

(5)

where I_m is the modified Bessel function of the first kind. Note the superscript on k_2^b which indicated the plate thickness inside the hole. The coefficients in the above two equations, a_m to h_m, determine the scattered field.

(2) Now that the scalar potential fields have been defined inside and outside the hole, the displacement field can be determined by the following expressions.

$$u_r^p = \frac{\partial \phi^p}{\partial r} + \frac{1}{r}\frac{\partial \psi^p}{\partial \theta} - z\frac{\partial w^p}{\partial r},$$

$$u_\theta^p = \frac{1}{r}\frac{\partial \phi^p}{\partial \theta} - \frac{\partial \psi^p}{\partial r} - \frac{z}{r}\frac{\partial w^p}{\partial r},$$

$$u_z^p = w^p,$$

(6)

where $p = (inc, >, <)$, represents the region being referred to, and $z \in (-h, h)$ for waves outside ($>$) the hole and $z \in (-b, b)$ for waves inside ($<$) the hole.

(3) The non-zero stresses are obtained from these displacements by the relation

$$\sigma_{rr}^p = \frac{E}{1-\nu^2}\left[\left(\frac{\partial}{\partial r} - \frac{\nu}{r}\right)u_r^p + \frac{\nu}{r}\frac{\partial}{\partial \theta}u_\theta^p\right]$$

$$\sigma_{r\theta}^p = \frac{E}{2(1+\nu)}\left[\left(\frac{\partial}{\partial r} - \frac{1}{r}\right)u_\theta^p + \frac{1}{r}\frac{\partial}{\partial \theta}u_r^p\right]$$

(7)

This can in turn be used to determine the forces on the plate, that is,

$$N_{rr}^p = \int_{-h}^{h} \sigma_{rr}^p dz, \quad N_{r\theta}^p = \int_{-h}^{h} \sigma_{r\theta}^p dz,$$

(8)

with moments

$$M_{rr}^p = \int_{-h}^{h} z\sigma_{rr}^p dz, \quad M_{r\theta}^p = -\int_{-h}^{h} z\sigma_{r\theta}^p dz,$$

(9)

where the domain of integration depends on the location on the plate. The final important quantity is the generalized Kirchhoff stress V_r that is determined by the twisting moment $M_{r\theta}$, defined as

$$V_r^p = -D\frac{\partial}{\partial r}\left(\Delta^2 w^p\right) - \frac{1}{r}\frac{\partial M_{r\theta}^p}{\partial \theta}.$$

(10)

(4) Finally having solved for the displacements, forces, moments and stresses, the coefficients $a_m \dots h_m$ for the scattered field can be determined, by enforcing the boundary conditions at $r = a$. The first boundary conditions to be enforced is the continuity condition of the in-plane displacements about the line $z' = 0$,

$$u_r^{inc} + \frac{\partial \phi^>}{\partial r} + \frac{1}{r}\frac{\partial \psi^>}{\partial \theta} + (h-b)\frac{\partial \omega^>}{\partial r} = \frac{\partial \phi^<}{\partial r} + \frac{1}{r}\frac{\partial \psi^<}{\partial \theta},$$

$$u_\theta^{inc} + \frac{1}{r}\frac{\partial \phi^>}{\partial \theta} - \frac{\partial \psi^>}{\partial r} + (h-b)\frac{1}{r}\frac{\partial \omega^>}{\partial \theta} = \frac{1}{r}\frac{\partial \phi^<}{\partial \theta} - \frac{\partial \psi^<}{\partial r}.$$

(11)

We also enforce continuity of the plates vertical displacement as well as its gradient

$$\omega^> = \omega^<,$$

$$\frac{\partial \omega^>}{\partial r} = \frac{\partial \omega^<}{\partial r}.$$

(12)

Finally, the forces, moments and stresses are balanced, we have

$$N_{rr}^{inc} + N_{rr}^> = N_{rr}^<,$$

$$N_{r\theta}^{inc} + N_{r\theta}^> = N_{r\theta}^<.$$

(13)

This continuity is not effected by the asymmetry due to the hole, however this asymmetry plays a role in the continuity of the generalized Kirchhoff stress and the bending moment. For this reason, the forces, moments and stresses are balanced as

$$V_r^> + \frac{1}{r}\frac{\partial}{\partial \theta}((h-b)N_{r\theta}^<) = V_r^<,$$

$$M_{rr}^> + (h-b)N_{rr}^< = M_{rr}^<.$$

(14)

By satisfying the above 8 boundary conditions we can solve for all 8 unknown coefficients $a_m, \ldots, h_m$ for every value of m by solving:

$$\begin{pmatrix} \alpha_{11} & \alpha_{12} & \alpha_{13} & \alpha_{14} & \alpha_{15} & \alpha_{16} & 0 & 0 \\ \alpha_{21} & \alpha_{22} & \alpha_{23} & \alpha_{24} & \alpha_{25} & \alpha_{26} & 0 & 0 \\ 0 & 0 & \alpha_{33} & \alpha_{34} & 0 & 0 & \alpha_{37} & \alpha_{38} \\ 0 & 0 & \alpha_{43} & \alpha_{44} & 0 & 0 & \alpha_{47} & \alpha_{48} \\ \alpha_{51} & \alpha_{52} & 0 & 0 & \alpha_{55} & \alpha_{56} & 0 & 0 \\ \alpha_{61} & \alpha_{62} & 0 & 0 & \alpha_{65} & \alpha_{66} & 0 & 0 \\ 0 & 0 & \alpha_{73} & \alpha_{74} & \alpha_{75} & \alpha_{76} & \alpha_{77} & \alpha_{78} \\ 0 & 0 & \alpha_{83} & \alpha_{84} & \alpha_{85} & \alpha_{86} & \alpha_{87} & \alpha_{88} \end{pmatrix} \begin{pmatrix} a_m \\ b_m \\ c_m \\ d_m \\ e_m \\ f_m \\ g_m \\ h_m \end{pmatrix} = \begin{pmatrix} \beta_{11} \\ \beta_{21} \\ 0 \\ 0 \\ \beta_{51} \\ \beta_{61} \\ 0 \\ 0 \end{pmatrix}. \quad (15)$$

The terms α_{ij} and β_{ij} are given explicitly in the appendix.

After solving for all 8 unknown coefficients $a_m, \ldots, h_m$ for a fixed m value, the scattered field of each wave mode can be determined. The scattered field is represented by $\mathbf{s}_{\mathcal{M}}(\boldsymbol{\lambda})$, which will be used in the next section to construct a Bayesian inference framework. Here, $\boldsymbol{\lambda}$ refers to unknown model parameters, including the radius and depth of the hole.

As mentioned at the beginning of this section, the inversion framework is computationally expensive. We performed the wave damage interaction model on a multicore server with Intel Xeon E5-1620 v4 Processor (3.50 GHz) and 32 GB of installed RAM. It is worth emphasizing that the presented semi-analytical approach only takes a few milliseconds per run to produce scattering features, which can greatly improve the calculation efficiency of the entire inversion process.

3. Description of scattering feature extraction

In physical experiments and finite element simulations, only raw signals are provided. Signal processing techniques need to be used to extract damage features. In this section, a signal processing technique for extracting scattering coefficients from ultrasonic signals is introduced. The scattering coefficients will be used as the available data $\mathcal{D}$ in Bayesian inversion.

Here, we take the signal from the physics experiment as an example to illustrate the signal processing part of the procedure. In order to explain it clearly, only one actuator and one sensor are considered, shown in Fig. 2. The red dot and blue square represent actuator and sensor, respectively. The purple dot represents a notch. d_1, d_2 and d_3 represents distance between different points. When the excitation frequency is 300 kHz, the time domain signal received by the sensor in the original state and the damaged state with the marked timeline of the Lamb wave is shown in Fig. 3. One can locate the modes by calculating the time for different modes to reach the sensor and the damage, which is shown on the vertical line in Fig. 3. One can determine the time-of-flight (ToF) Δt of certain modes by dividing the distance by the propagation speed of a certain mode wave:

$$\Delta t = \frac{d}{V_{(S0/A0)}} \quad (16)$$

where $V_{(S0/A0)}$ and d denote the speed of S0 or A0 modes and the distance, respectively. When calculating the ToF of incident waves, the distance is taken as d_1. When calculating the ToF of the scattered wave, the distance is taken as the sum of d_2 and d_3. When the material parameters and excitation frequency are known, the speed of different waves can be calculated using the Dispersion Calculator [44]. The scattered S0 and A0 waves are clearly separated, which helps in calculating the scattering coefficient more accurately.

The scattering coefficients can be calculated in the time or frequency domain [21,45,46]. In this study, the frequency domain technique is adopted. The coefficients were computed by dividing the frequency spectra of the reflected/transmitted part of the signal by that of the incident part. It is straightforward to obtain the frequency spectra of the incident waves. For the scattering part, the difference in propagation time of different types of wave modes is used to identify the corresponding scattering bands. Then, the scattering bands in the time domain were transformed with fast Fourier transform. The above

process was repeated on each sensor (see Fig. 4). To this end, the scattering contour was obtained, which contains the information of the defects. The extracted features will be used in the next section to infer the size of the damages.

4. Damage characterization

Bayesian inference provides a rigorous probabilistic framework for solving inverse problems with quantified uncertainties. More specifically, measurement noise and modelling errors can be quantified, and one can fully make use of prior information (for example, ultrasonic monitoring data) through this framework [47]. The Bayesian framework for identifying the radius and depth of a hole in plate like structures is presented based on frequency-domain data derived from Section 2.

4.1. Probabilistic model class construction

The deterministic wave damage interaction model $\mathcal{M}$ presented in Section 2 provides the scattering coefficients, denoted as $\mathbf{s}_{\mathcal{M}}(\boldsymbol{\lambda}) \in \mathbb{R}^{N_s}$. N_s refers to the dimension of scattering coefficients. The experimental scattering coefficients $\mathbf{s}_{\mathcal{D}} \in \mathbb{R}^{N_s}$ are derived from the output of ultrasonic experiment and contain the necessary information to characterize damage by identifying its damage parameters. The model is dependent on a set of unknown model parameters $\boldsymbol{\lambda} \in \Theta \subset \mathbb{R}^{N_\theta}$, including the radius and depth of damage. N_θ refers to the dimension of scattering coefficients. The probabilistic damage interaction model is defined by introducing an error term $\mathbf{e} \in \mathbb{R}^{N_s}$ that accounts for the discrepancy between the modelled coefficients $\mathbf{s}_{\mathcal{M}}(\boldsymbol{\lambda})$ and the coefficients derived from experiments, that is $\mathbf{s}_{\mathcal{D}}$, as follows:

$$\mathbf{s}_{\mathcal{D}} = \mathbf{s}_{\mathcal{M}}(\boldsymbol{\lambda}) + \mathbf{e}. \quad (17)$$

A zero mean Gaussian distribution with covariance matrix $\Sigma_e = \text{diag}(\sigma_{e,1}^2, \sigma_{e,1}^2, \ldots, \sigma_{e,N_s}^2)$ is selected to model the error term in order to produce the largest prediction uncertainty, i.e., $\mathbf{e} \sim \mathcal{N}(0, \Sigma_e)$. This is based on the principle of Maximum Information Entropy [48,49]. The stochastic version of the model is given by a Gaussian distribution

$$p\left(\mathbf{s}_{\mathcal{D}} | \mathbf{s}_M, \boldsymbol{\lambda}, \mathcal{M}\right) = \left(2\pi\sigma_e^2\right)^{-\frac{N_s}{2}} \exp\left(-\frac{1}{2}\left(\frac{\mathcal{J}(\boldsymbol{\lambda}, \mathcal{D})}{\sigma_e}\right)^2\right), \quad (18)$$

where $\mathcal{J}(\boldsymbol{\lambda}, \mathcal{D})$ is a goodness-of-fit function which is selected to be the L_2-norm of the experimental and modelled data defined as

$$\mathcal{J}(\boldsymbol{\lambda}, \mathcal{D}) = \left(\sum_{i=1}^{N_s}(s_{\mathcal{M},i} - s_{\mathcal{D},i})^2\right)^{1/2} \quad (19)$$

with $s_{\mathcal{M},i}$ and $s_{\mathcal{D},i}$ being the ith element of the vectors $\mathbf{s}_M$ and $\mathbf{s}_{\mathcal{D}}$, respectively.

4.2. Bayesian inference

The posterior probability is the state of knowledge of the distribution of the model parameters after updating the prior information with the measurement data $\mathcal{D}$. The posterior distribution of the model parameters $p(\boldsymbol{\lambda}|\mathcal{D}, \mathcal{M})$ can be obtained from the prior probability density function (PDF) $p(\boldsymbol{\lambda}|\mathcal{M})$ by applying Bayes' theorem, given the data $\mathcal{D} \triangleq \mathbf{s}_{\mathcal{D}}$, that is,

$$p(\boldsymbol{\lambda}|\mathcal{D}, \mathcal{M}) = \frac{p(\mathcal{D}|\boldsymbol{\lambda}, \mathcal{M})\, p(\boldsymbol{\lambda}|\mathcal{M})}{p(\mathcal{D}|\mathcal{M})}, \quad (20)$$

where $p(\mathcal{D}|\boldsymbol{\lambda}, \mathcal{M})$ is the likelihood function given by Eq. (18) and the denominator $p(\mathcal{D}|\mathcal{M})$ is known as the evidence and is a measure of how well the model explains the data $\mathcal{D}$. It acts as a normalization constant in Bayes' theorem. The prior PDF $p(\boldsymbol{\lambda}|\mathcal{M})$ is the state of knowledge before any measurement is available.

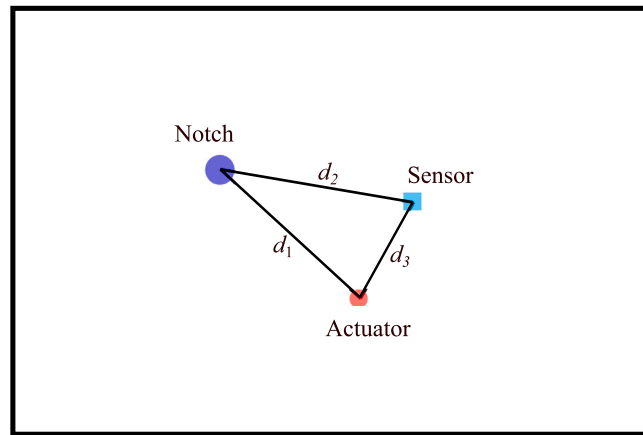**Fig. 2.** Actuator and sensor allocation with geometry information. The red dot, blue square, and purple dot represent actuator, sensor and notch, respectively. d_1, d_2 and d_3 represents distance between different points.
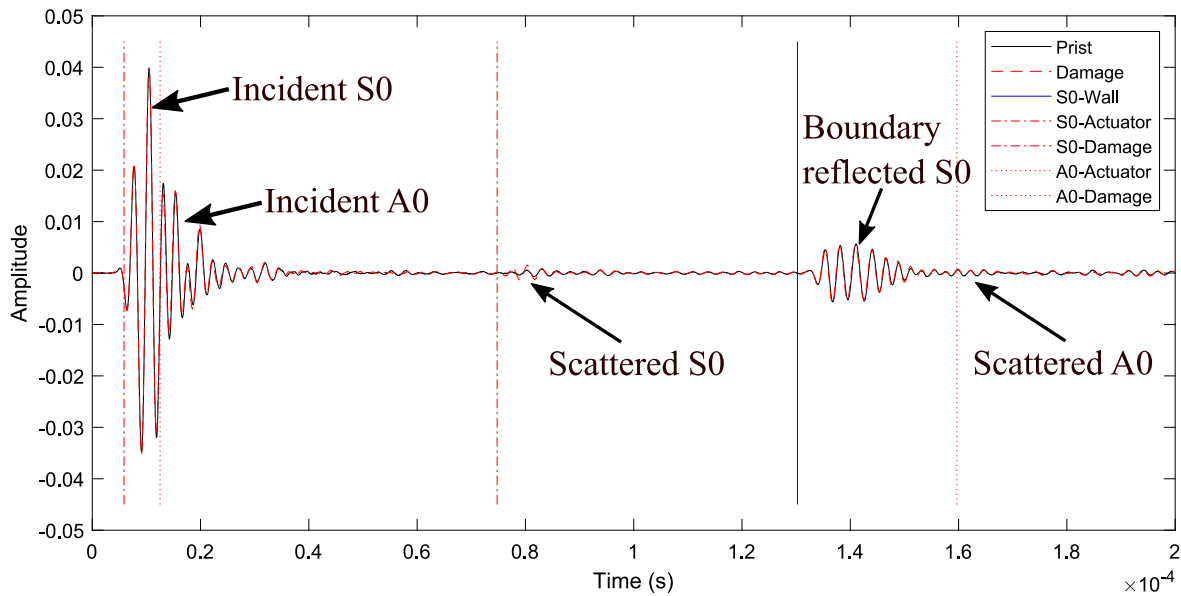

Fig. 3. Time domain signal of pristine and damage state in 300 kHz in 0.9 mm aluminium plate with marked timelines of Lamb wave. The timelines are calculated according to Eq. (16), which can used to locate and separate different Lamb wave modes. Note that the signals are obtained by ultrasonic guided waves tests.

The evaluation of Eq. (20) requires the calculation of multi-dimensional integrals which is not possible in practical applications. Markov Chain Monte Carlo (MCMC) methods [50] have been widely used for their ability to estimate the posterior PDF while this approach makes it possible to obtain samples directly from the posterior distribution and bypassing the computation of the evidence. Out of the vast amount of MCMC algorithms available in the literature, the Metropolis–Hastings (M–H) algorithm [51,52] is used here as a stochastic simulation method given its versatility and its ease of implementation [47]. It is worth noting that a Gaussian distribution $q(\lambda'|\lambda^\zeta)$ is chosen as the proposal in the M–H algorithm, which can influence the speed of convergence of the algorithm, see Appendix A for more details. In an M–H algorithm, the posterior PDF is characterized by the posterior samples λ^ζ. The value range of ζ is 1 to T_s. T_s refers to the number of samples. Based on this, the multi-dimensional integral can be approximated by the following expression:

$$p\left(\lambda'|\mathscr{D},\mathscr{M}\right) \approx \frac{1}{T_s} \sum_{\zeta=1}^{T_s} p\left(\lambda' \mid \lambda^{(\zeta)}, \mathscr{D}, \mathscr{M}\right). \tag{21}$$

For the sake of clarity, a generic algorithmic implementation is provided in Fig. 5.

5. Case studies

5.1. Numerical example

In this section, a numerical case study of a steel plate with a part-depth circular hole is presented. The experimental data $\mathscr{D}$ is generated by performing a full finite element simulation in Abaqus and post-processing the output displacements to obtain the scattering coefficients. The schematic for the numerical simulation is shown in Fig. 6.

The dimension of the specimen is $L_x = 900$ mm x $L_y = 800$ mm in size and 2 mm in thickness. The material properties for steel are as follows: elastic modulus $E = 210$ GPa, density $\rho = 8100$ kg/m³ and Poisson ratio $v = 0.3$. A 1 mm deep circular indentation is modelled at the centre of the plate with radius 5 mm. An incident plane wave of fundamental S0 mode is generated by applying a transient force to the entire boundary as shown in Fig. 6. The forcing function is a 6 cycle Hanning windowed sinusoid with a central frequency of 100.514 kHz and a time duration of 60 μs. The model is meshed by using 8-node general purpose linear brick elements (C3D8R) [53], with reduced integration and maximum element edge length of 1 mm.
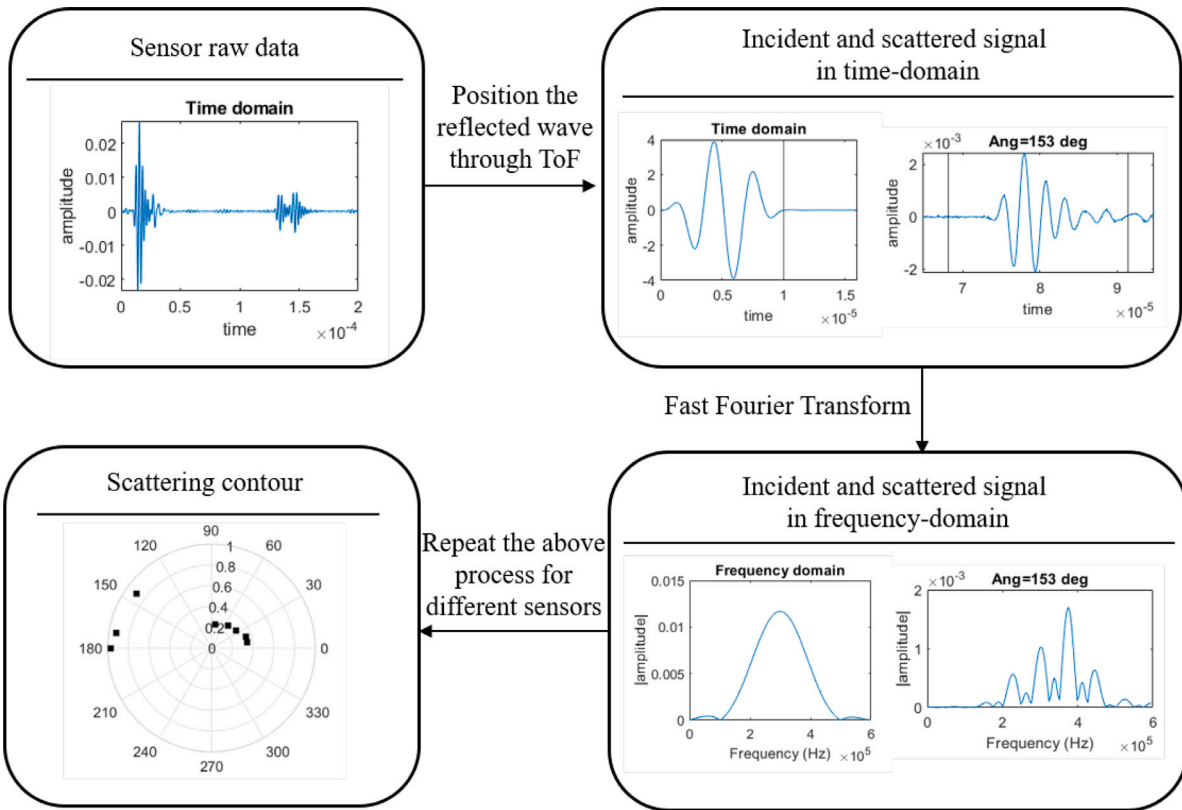
Fig. 4. Scheme of signal processing to obtain scattering coefficients. Note that the signal data can be obtained by numerical (e.g. FEM) or experimental methods (e.g. using PZT transducers, a signal generator, and an oscilloscope).
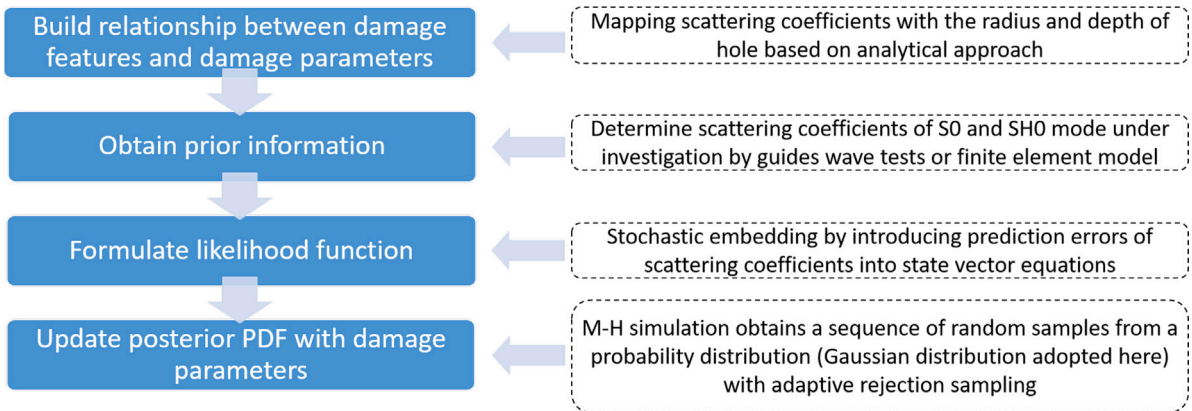

Fig. 5. General workflow of Bayesian inference for damage identification.

A circular monitoring contour is specified in the vicinity of the damage. This consists of nodes at which the displacement components are observed. The radius of the monitoring contour must be large enough to ensure at least one wavelength separation from the damage. Then the displacements recorded at these nodes can be considered in the far-field of the damage. There are two simulations necessary with this approach. First a plate without damage is simulated and the displacements components are stored. After that a simulation is executed with damage in the plate and again the displacements are stored. The same signal processing method describe in Section 3 is adopted here to obtain scattering coefficients. The scattered portion of the displacements is obtained by subtracting the displacements from the two simulations. The normalized far-field displacement components in the cylindrical coordinate system are the scattering coefficients used as the experimental data $\mathscr{D}$.

Table 1
Identified results of the numerical case.

Parameters	True value	MAP	Mean	Std	COV(%)
a (mm)	5.0	4.9238	4.9369	1.7248e−4	2.9751e−06
b (mm)	0.5	0.4959	0.5003	1.9927e−5	3.9709e−08
σ_e	–	0.0317	0.0333	0.0043	1.8614e−03

A uniform prior distribution was used with bounds [0.0035 mm, 0.0065 mm] for radius a, [0.00001 mm, 0.001 mm] for depth b and [0.0001, 0.1] for standard deviation σ_e. Similarly, samples from the posterior PDFs of each set of model parameters are obtained through the M–H algorithm (refer to the Appendix) using 100,000 samples and a Gaussian proposal distribution. The resulting marginal posterior PDFs are described in Table 1 by their maximum a posteriori value (MAP),
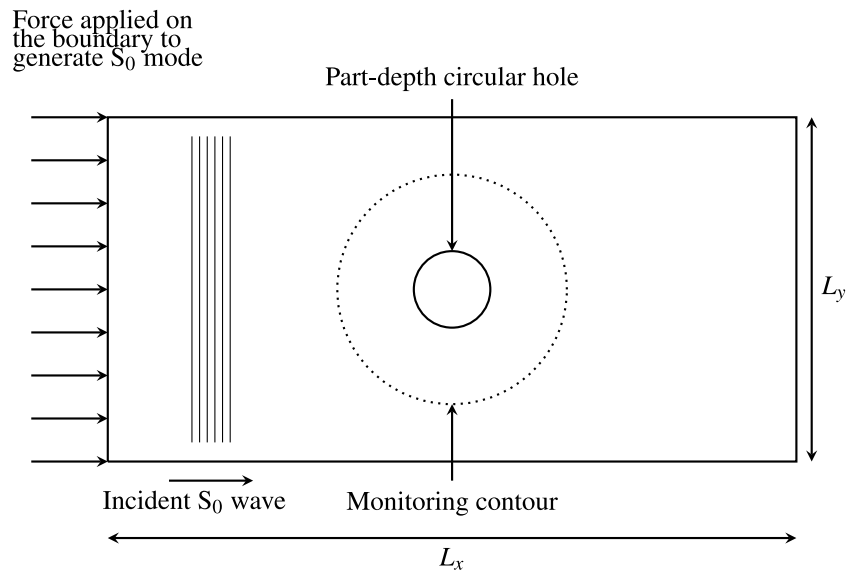
Fig. 6. Schematic of the finite element simulation model for extraction of scattering coefficients. Two simulations (pristine and damage state) are required with this approach. The signal obtained by the simulation will be processed according to the method in Section 3.
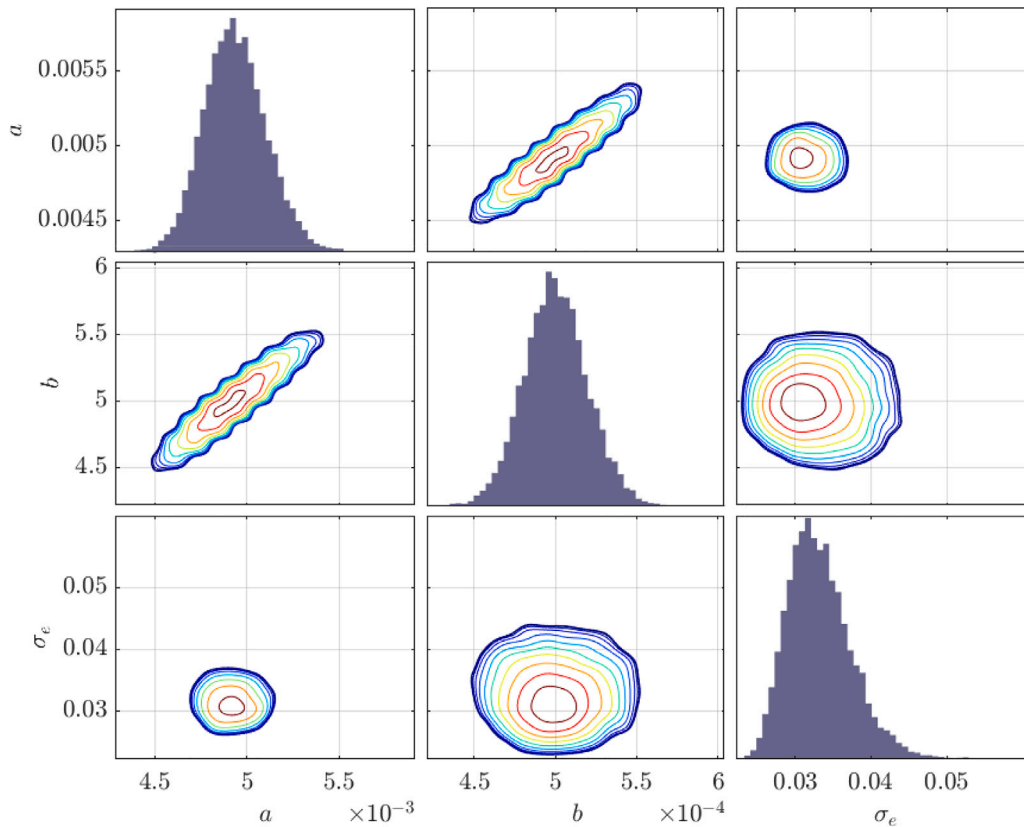

Fig. 7. Posterior distribution of different parameters and contours of two-dimensional simulation densities inferred from full finite element model. Diagonal plots indicate the marginal distributions of the inferred parameters.

their mean, their standard deviation (Std), and their coefficients of variation (COV). Fig. 7 shows the posterior distribution of identified parameters and contours of two-dimensional simulation densities.

For the numerical case, in terms of MAP, the corresponding errors of the radius and the depth are 1.52% and 0.82% respectively. The inferred radius and depth has a good correlation to the true value. The comparison of the reconstructed scattering coefficients of S0 and SH0 mode using the MAP values of the posterior PDFs and the numerical

data is shown in Fig. 8. As shown, the model is able to reconstruct the contours of S0 and SH0. For S0 mode, between the values of 180° and 60° the reconstructed scattering coefficients are greater than the true value, below these values the opposite is true. Again, there is strong correlation between the reconstructed and true values, while a phase difference occurs for SH0 mode.

The Bayesian inference procedure is performed on a multicore server with the same scenarios mentioned in Section 2. The time
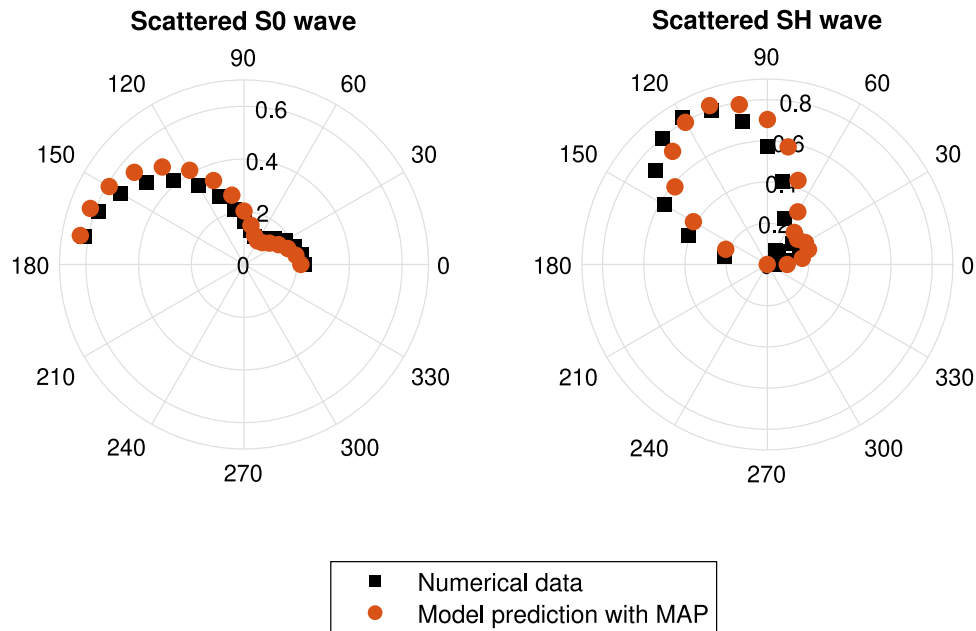
Fig. 8. Reconstruction of the scattering coefficients of S0 and SH0 mode based on the MAP values of the posterior PDF.

consumption of the whole Bayesian inversion is around 340 s. The semi-analytical method adopted in this paper narrows the scope of application to the problem of spherical symmetry. Therefore, compared with the traditional explicit finite element method, the calculation efficiency has been greatly improved. One can use the explicit finite element model as a benchmark to highlight the high efficiency of the proposed framework. The time taken for a single run of the explicit finite element model is around 95 min. If the full finite element model is used as the physical model to construct the Bayesian inversion framework, giving a total time taken of 9.5 million minutes (around 6597 days) for 100,000 samples. The framework used in this work is about 1,676,470 times more efficient than the one based on explicit finite element model. The framework eliminates the quagmire of time-consuming damage characterization based on the Bayesian method of physical model. In addition, it will significantly reduce the time expended for practical engineering application, such as determining maintenance strategies faster based on how the severity of identified damage. The main limitation of the proposed framework is that the identified damage is assumed to be spherically symmetric, so the numerical modelling of the Hankel and Bessel functions can be reduced to a fixed index 'm', leading to a low dimensional matrix problem; but such defect forms are very representative in metal structures. In the following work, we will explore the generalization of the method using non-uniform depth profiles.

5.2. Experimental study and damage identification through a digital-twin approach

In this section, an experimental case study of an aluminium plate with a part-depth circular hole is presented to validate the proposed framework in a hybrid cyber–physical environment. The experimental data $\mathscr{D}$ are generated by performing ultrasonic experiments.

The plate has the dimensions $L_x = 1000$ mm, $L_y = 1000$ mm and a depth of 0.9 mm with the properties of the aluminium plate detailed in Table 2. The defect is located in the centre of the plate to ensure dissipation of the reflected waves from the boundaries. The configuration of different piezoelectric (PZT) sensors is shown in Fig. 9. The red PZT has been used to generate a sinusoidal burst, and the rest of the PZT sensors received the reflected and scattered signals. PZT sensors are 7 mm in diameter and 0.2 mm in thickness with radial

Table 2
Mechanical properties of aluminium plate.

Thickness (mm)	Young's modulus (GPa)	Poisson's ratio	Density (kg/m^3)
0.9	69	0.33	2705

mode vibration and a resonant frequency of 300 kHz. PZT sensors are mounted on the structure's surface radially with equal spacing. A Keysight 33512B arbitrary waveform generator was used to generate a five-cycle sine tone-burst centred in a specific frequency range, and a DSOX2014 A oscilloscope was used to digitize the signals using a sampling frequency of 9.6 MHz and averaging 32 measurements to increase the signal-to-noise ratio. The experimental setup is shown in Fig. 10.

The semi-analytical method presented in Section 2 considers the excitation with an S0 wave, and the scattered field as S0, A0 and SH0 waves. In order to more accurately characterize the interaction between different modal waves and defects, the strengthening of the incident S0 mode and the weakening of other incident modes is required for the experiment to verify the theoretical model.

In this paper, the impact of A0 was minimized by using three complimentary methods. First, avoid appearance of higher modes and enhance the incident S0 mode. As mentioned in Section 2, the excitation frequency is lower than the cutoff frequency to avoid the appearance of higher-order modes, however, the choice of the excitation mode (S0 and A0) is an important task. Different approaches are used to select guided wave modes, including dual PZT excitation [54, 55], PZT array excitation [56,57], choosing frequency range [58,59]. In our experiments, the exciting frequency range from 120 kHz to 300 kHz is explored. The time domain signal of the sensor closest to the actuator in 120 kHz, 180 kHz, 240 kHz, 300 kHz are shown in Fig. 11. The time-of-arrival is used to locate incident S0 and A0. It is observed that with the increase of frequency, the amplitude of incident S0 is enhanced; at 300 kHz, the maximum amplitude of S0 is more than twice that of A0. Note that mode selection approaches can be used to enhance a specific Lamb wave mode at a given frequency while minimizing the contribution of others modes, but they cannot remove a wave mode in a signal completely [54]. Therefore, 300 kHz is finally selected as an exciting frequency. Besides, to ensure that the scattered S0 and A0 are
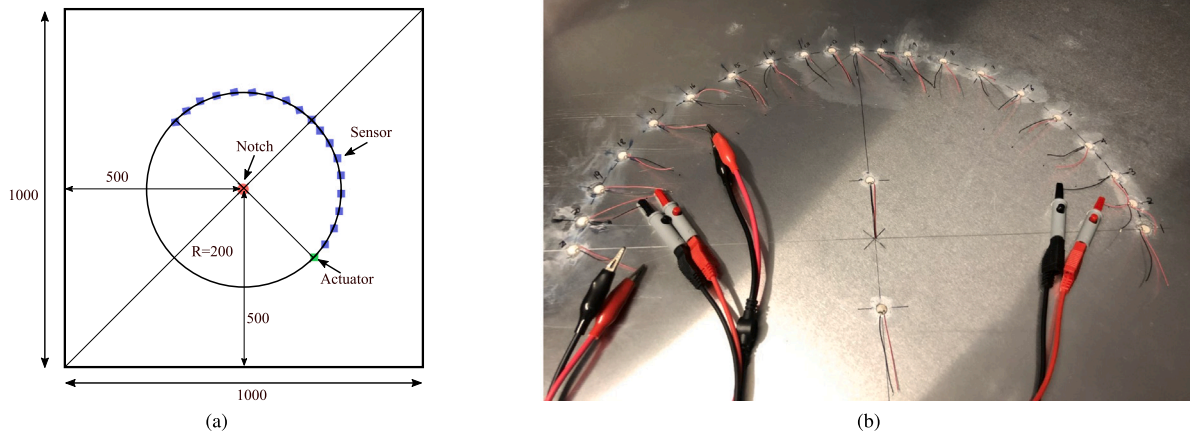
Fig. 9. (a) Plate geometry and sensor allocation. (b) experimental configuration (units in mm). PZT sensors are mounted on the structure's surface radially with equal spacing. The square and red dot represent sensors and notch, respectively.
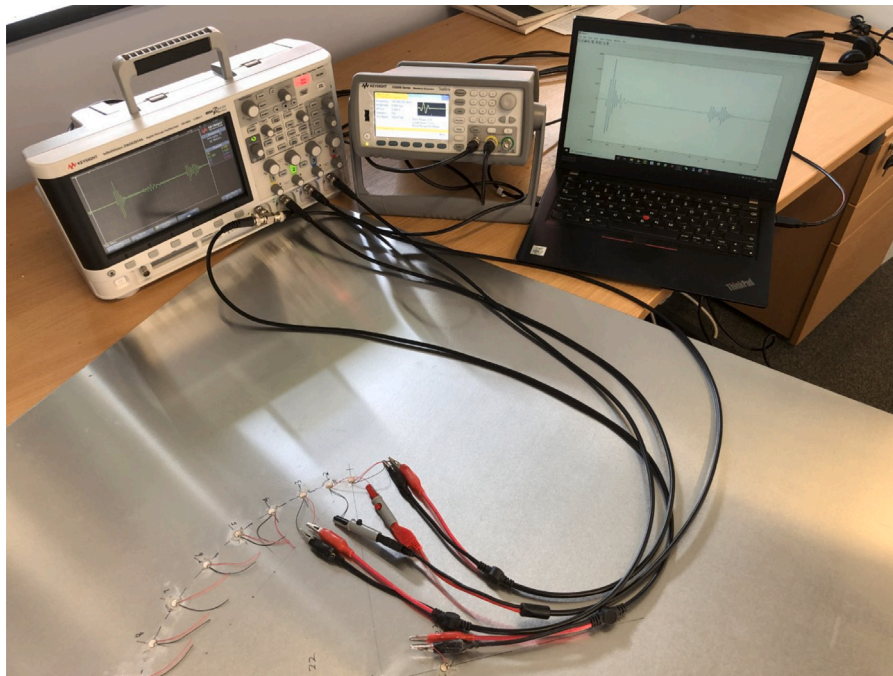

Fig. 10. Experiment setup used comprising a laptop, an arbitrary waveform generator and an oscilloscope connected to the PZT transducers attached to the aluminium plate.

separated, there is a limit to the minimum distance between the sensor and the defect:

$$\frac{d_{minimum}}{V_{A0}} - \frac{d_{minimum}}{V_{S0}} \geq n * \frac{1}{f} \tag{22}$$

where $d_{minimum}$ represents the minimum distance between the sensor and the defect. n represents the exciting cycle. f represents the exciting frequency. For example, under the condition of an incident wave with 3 cycles at 300 kHz, calculated according to Eq. (22), the minimum distance is 47.29 mm. In our set-up, the distance between the sensor and the defect is 200 mm, which is greater than the minimum distance; as shown in Fig. 3, scattered A0 and S0 are clearly separated. Furthermore, as mentioned in Section 3, frequency domain scattering coefficient calculation method is adopted. The coefficients are calculated by dividing the peak value of the frequency spectrum of the reflected part of the signal by the peak value of the frequency spectrum of the incident part [45,46], see Fig. 4. As mentioned above, the maximum amplitude of S0 is much greater than that of A0, so the impact of A0 is minimized as much as possible.

The scattering coefficients obtained from the physical experiments of the aluminium panel with a circular notch is assessed with the proposed Bayesian framework to identify the radius and the depth thus validating the feasibility of the framework in real applications. A uniform prior distribution was used with bounds [0.0015 m, 0.0045 m] for radius a, [0.0001 m, 0.0004 m] for depth b and [0.01, 0.1] for standard deviation σ_e. Samples from the posterior PDFs of each set of model parameters are obtained through the M–H algorithm (refer to the Appendix) using 100,000 samples and a Gaussian proposal distribution. The identified results including mean values, MAP(maximum a posteriori value), standard deviation(Std) and COV(Coefficients of variation) are presented in Table 3. Fig. 12 shows the posterior distribution of identified parameters and contours of two-dimensional simulation densities. The identified radius of the circular hole are very close to the true values. The corresponding errors of the radius and the depth in terms of MAP are 1.68% and 25.0% respectively. However, there is the discrepancy between the identified hole depth and the measured hole depth. It should be pointed out that in real tests, the bottom of the defect is rarely flat. Therefore, the true value of the defect depth
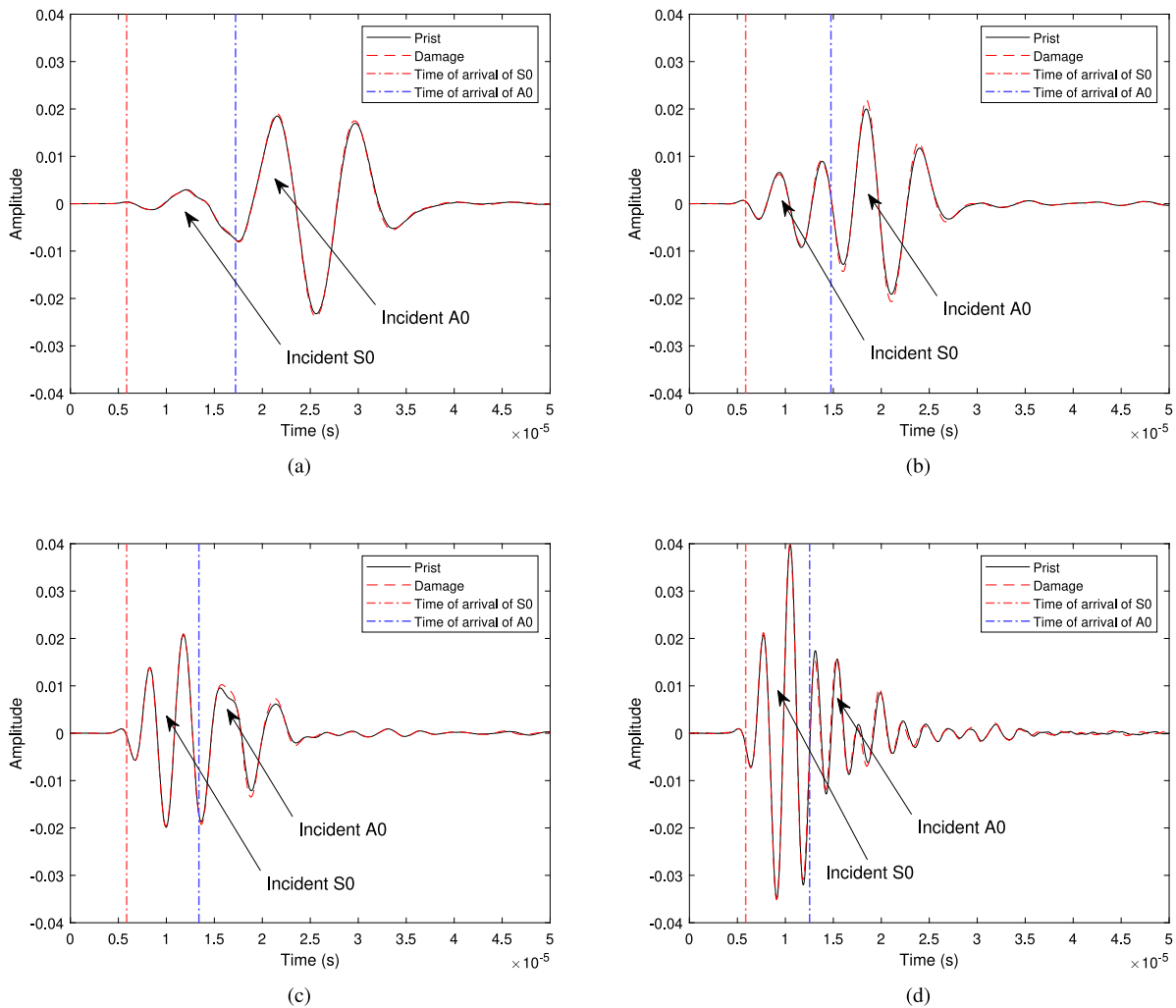
Fig. 11. Time domain signal of pristine and damage state in 0.9 mm aluminium plate in (a) 120 kHz, (b) 180 kHz, (c) 240 kHz and (d) 300 kHz; the incident wave S0 and A0 are highlighted.

Table 3
Identified results of the physical experiment.

Parameters	True value	MAP	Mean	Std	COV(%)
a (mm)	3.25	3.3045	3.2606	1.6769e−04	2.8121e−06
b (mm)	0.2	0.2499	0.2505	4.4010e−6	1.9369e−09
σ_e	–	0.02605	0.0329	0.0120	1.4482e−02

here is the average value of the defect depth, which has an impact on the accuracy of the inversion depth. After the further extension of the semi-analytical method adopted in this paper, the above case can also be simulated. While the current characterization results already have practical guiding significance, further methods will not be discussed here.

In addition, the MAP values of the posterior PDF are used to reconstruct the scattering coefficients of the S0 mode, and these coefficients are compared with the numerical data (see Fig. 13). Discrepancy between the reconstructed scattering coefficients and the measured values is observed. Whilst the shape is quite similar, there is a more distinct difference as the angle approaches zero. This difference is due to model errors caused by the inconsistency between the ideal structure model in the semi-analytical approach and the actual specimen in the experiment, such as the difference in material properties, the difference in damping and dispersion, and the difference between the hole shape and the actual one. However, this is expected in a practical scenario,

but that the actual characterization of the defect is sufficiently accurate for most of the applications with the errors being in the order of 0.1 mm. Overall, the Bayesian inference framework based semi-analytical approach yielded sufficient damage identification capability to warrant further investigation into field application.

6. Conclusions

In summary, a Bayesian inference framework for damage identification of plate structures with spherical symmetry is presented where a guided waves interaction model is used based on a semi-analytical approach. It combines Poisson theory and Kirchhoff theory producing the scattered field when a plane S0 wave forms the incident wave on a plate defect. The proposed framework is finally validated by a physical experiment and a full finite element model. The high-efficient framework shows excellent promise to build a fast digital twin that will be connected to the physical twin to support real-time engineering decisions by capturing the impact of detected damage on structural performance and remaining useful life. The following conclusions are draw from this paper:

- A fast Lamb-wave based physics-informed damage identification framework in 2D structures for the first time is proposed, which can identify the geometry of a partly through-thickness circular hole in plate-like structures. The scattering coefficients of Lamb
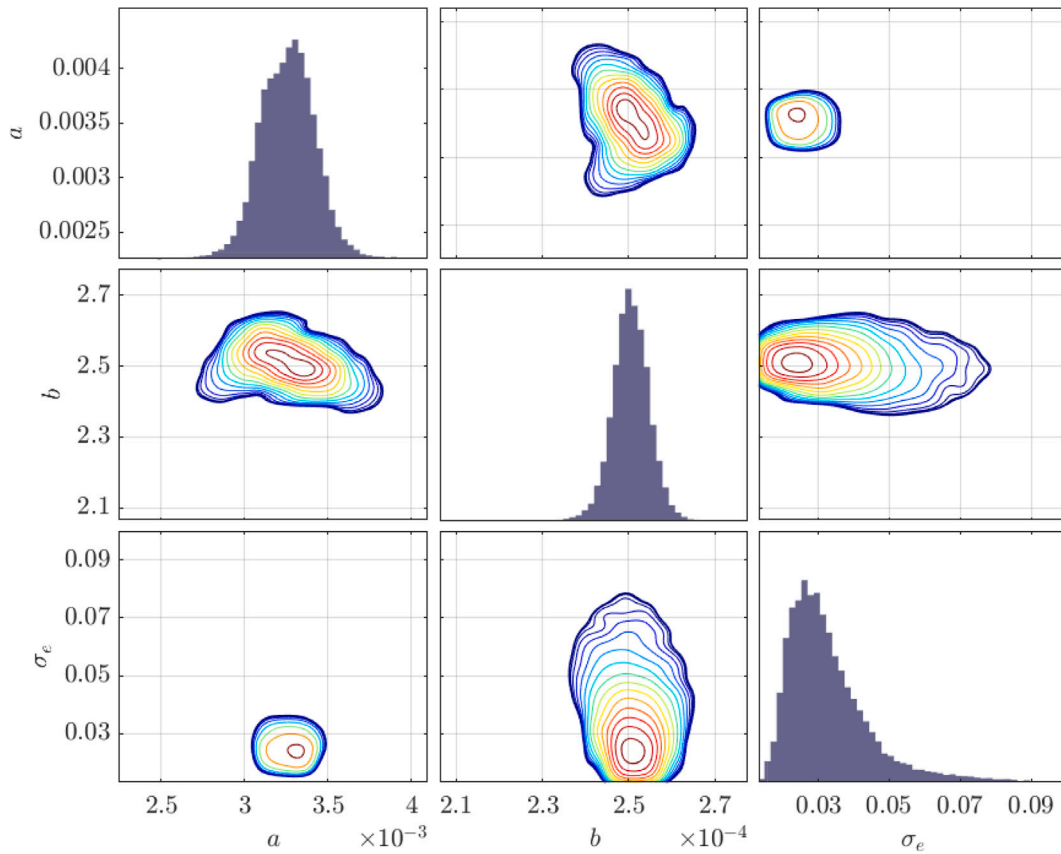
Fig. 12. Posterior distribution of different parameters and contours of two-dimensional simulation densities inferred from physical experiments. Diagonal plots indicate the marginal distributions of the inferred parameters.
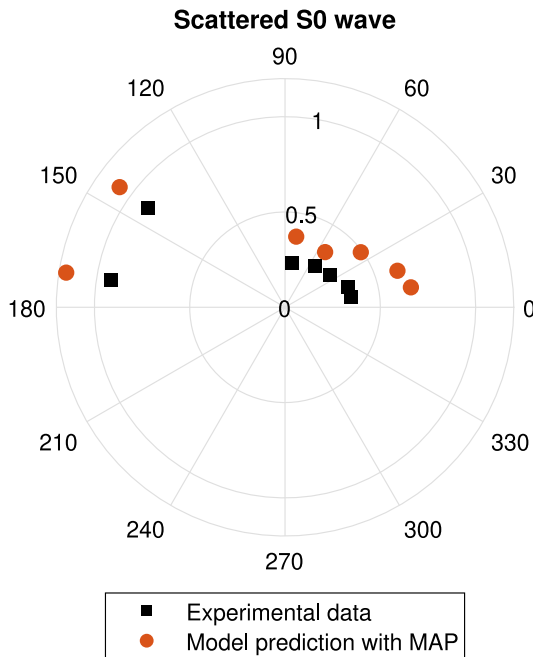

Fig. 13. Reconstruction of the scattering coefficients of S0 mode based on the MAP values of the posterior PDF.

wave modes are reconstructed, and there is strong correlation between the reconstructed and true values.

- Compared with a traditional finite element model and similar methods, the presented semi-analytical approach can greatly improve the robustness and efficiency of the inversion procedure for a spherically symmetry damage without introducing more epistemic uncertainty.
- Physical ultrasound experiments for large Aluminium plate are conducted to extract wave reflection, transmission coefficients with the aid of signal processing techniques. The use of features in the frequency domain have clear physical meaning and are more computationally efficient than the time domain approaches.

CRediT authorship contribution statement

W. Wu: Conceptualization, Methodology, Software, Validation, Formal analysis, Writing – original draft, Writing – review & editing, Visualization. **M.K. Malik:** Conceptualization, Methodology, Software, Writing – review & editing, Supervision. **S. Cantero-Chinchilla:** Conceptualization, Methodology, Software, Writing – review & editing, Supervision. **T. Lawrie:** Conceptualization, Methodology, Writing – review & editing, Supervision. **W.J. Yan:** Conceptualization, Supervision. **G. Tanner:** Writing – review & editing, Supervision. **R. Remenyte-Prescott:** Funding acquisition, Project administration, Supervision. **D. Chronopoulos:** Conceptualization, Funding acquisition, Resources, Investigation, Writing – review & editing.

Declaration of competing interest

The authors declare that they have no known competing financial interests or personal relationships that could have appeared to influence the work reported in this paper.

Appendix A. Metropolis–Hastings simulation for Bayesian updating

The M–H algorithm generates samples from a specially constructed Markov chain whose stationary distribution is the required posterior PDF $p(\boldsymbol{\lambda}|\mathscr{D}, \mathcal{M})$. By sampling a candidate model parameter $\boldsymbol{\lambda}'$ from a *proposal distribution* $q(\boldsymbol{\lambda}'|\boldsymbol{\lambda}^\zeta)$, the M–H obtains the state of the chain at $\zeta + 1$, given the state at ζ, specified by $\boldsymbol{\theta}^\zeta$. The candidate parameter $\boldsymbol{\lambda}'$ is accepted (i.e., $\boldsymbol{\lambda}^{\zeta+1} = \boldsymbol{\lambda}'$) with probability $\min\{1, r\}$, and rejected (i.e., $\boldsymbol{\lambda}^{\zeta+1} = \boldsymbol{\lambda}^\zeta$) with the remaining probability $1 - \min\{1, r\}$, where:

$$r = \frac{p(\mathscr{D}|\boldsymbol{\lambda}', \mathcal{M})p(\boldsymbol{\lambda}'|\mathcal{M})q(\boldsymbol{\lambda}^{\zeta-1}|\boldsymbol{\lambda}')}{p(\mathscr{D}|\boldsymbol{\lambda}^{\zeta-1}, \mathcal{M})p(\boldsymbol{\lambda}^{\zeta-1}|\mathcal{M})q(\boldsymbol{\lambda}'|\boldsymbol{\lambda}^{\zeta-1})} \tag{A.1}$$

The process is repeated until T_s samples have been generated so that the monitored acceptance rate (ratio between accepted M–H samples over total amount of samples) reaches an asymptotic behaviour. A pseudo-code description of this method is provided below as Algorithm 1.

Algorithm 1: M–H algorithm

---

1   Initialize $\boldsymbol{\lambda}^{\zeta=0}$ by sampling from the prior PDF: $\boldsymbol{\lambda}^0 \sim p(\boldsymbol{\lambda}|\mathcal{M})$;
2   **for** $\zeta = 1$ **to** T_s **do**
3   Sample from the proposal: $\boldsymbol{\lambda}' \sim q(\boldsymbol{\lambda}'|\boldsymbol{\lambda}^{\zeta-1})$;
4   Compute r from Eq. (A.1);
5   Generate a uniform random number: $\alpha \sim \mathcal{U}[0, 1]$;
6   **if** $r \geqslant \alpha$ **then**
7   Set $\boldsymbol{\lambda}^\zeta = \boldsymbol{\lambda}'$;
8   **else**
9   Set $\boldsymbol{\lambda}^\zeta = \boldsymbol{\lambda}^{\zeta-1}$;
10   **end**
11   **end**

Appendix B. Coefficients required for the wave damage interaction model

The expansion coefficients in Eq. (15) are shown below. These parameters are used to solve all 8 unknown coefficients and obtain a scattered field.

$$\alpha_{11} = (k_1 a)H'_m(k_1 a), \quad \alpha_{12} = im H_m(k_T a), \quad \alpha_{13} = \left(1 - \frac{b}{h}\right)(k_2^h a)H'_m(k_2^h a),$$

$$\alpha_{14} = \left(1 - \frac{b}{h}\right)(k_2^h a)K'_m(k_2^h a), \quad \alpha_{15} = -(k_1 a)J'_m(k_1 a), \quad \alpha_{16} = -im J_m(k_T a). \tag{B.1}$$

$$\alpha_{21} = im H_m(k_1 a), \quad \alpha_{22} = -(k_T a)H'_m(k_T a), \quad \alpha_{23} = im\left(1 - \frac{b}{h}\right)H_m(k_2^h a),$$

$$\alpha_{24} = im\left(1 - \frac{b}{h}\right)K_m(k_2^h a), \quad \alpha_{25} = -im J_m(k_1 a), \quad \alpha_{26} = (k_T a)J_m(k_T a). \tag{B.2}$$

$$\alpha_{33} = H_m(k_2^h a), \quad \alpha_{34} = K_m(k_2^h a), \quad \alpha_{37} = -J_m(k_2^b a), \quad \alpha_{38} = -I_m(k_2^b a). \tag{B.3}$$

$$\alpha_{43} = (k_2^h a)H'_m(k_2^h a), \quad \alpha_{44} = (k_2^h a)K'_m(k_2^h a), \quad \alpha_{47} = -(k_2^b a)J'_m(k_2^b a),$$

$$\alpha_{48} = -(k_2^b a)I'_m(k_2^b a). \tag{B.4}$$

$$\alpha_{51} = \left(m^2 - \frac{(k_1 a)^2}{1-\nu}\right)H_m(k_1 a) - (k_1 a)H'_m(k_1 a),$$

$$\alpha_{52} = im[(k_T a)H'_m(k_T a) - H_m(k_T a)],$$

$$\alpha_{55} = -\frac{b}{h}\left[\left(m^2 - \frac{(k_1 a)^2}{1-\nu}\right)J_m(k_1 a) - (k_1 a)J'_m(k_1 a)\right],$$

$$\alpha_{56} = -im\frac{b}{h}[(k_T a)J'_m(k_T a) - J_m(k_T a)]. \tag{B.5}$$

$$\alpha_{61} = im[(k_1 a)H'_m(k_1 a) - H_m(k_1 a)],$$

$$\alpha_{62} = \left(\frac{(k_T a)^2}{2} - m^2\right)H_m(k_T a) + (k_T a)H'_m(k_T a),$$

$$\alpha_{65} = -im\frac{b}{h}[(k_1 a)J'_m(k_1 a) - J_m(k_1 a)],$$

$$\alpha_{66} = -\frac{b}{h}\left[\left(\frac{(k_T a)^2}{2} - m^2\right)J_m(k_T a) + (k_T a)J'_m(k_T a)\right]. \tag{B.6}$$

$$\alpha_{83} = -\frac{2}{3}\left[\left(m^2 - \frac{(k_2^h a)^2}{1-\nu}\right)H_m(k_2^h a) - (k_2^h a)H'_m(k_2^h a)\right],$$

$$\alpha_{84} = -\frac{2}{3}\left[\left(m^2 + \frac{(k_2^h a)^2}{1-\nu}\right)K_m(k_2^h a) - (k_2^h a)K'_m(k_2^h a)\right],$$

$$\alpha_{85} = 2\left(1 - \frac{b}{h}\right)\frac{b}{h}\left[\left(m^2 - \frac{(k_1 a)^2}{1-\nu}\right)J_m(k_1 a) - (k_1 a)J'_m(k_1 a)\right],$$

$$\alpha_{86} = 2\left(1 - \frac{b}{h}\right)\frac{b}{h}im[(k_T a)J'_m(k_T a) - J_m(k_T a)],$$

$$\alpha_{87} = \frac{2}{3}\left(\frac{b}{h}\right)^3\left[\left(m^2 - \frac{(k_2^b a)^2}{1-\nu}\right)J_m(k_2^b a) - (k_2^b a)J'_m(k_2^b a)\right],$$

$$\alpha_{88} = -\frac{2}{3}\left(\frac{b}{h}\right)^3\left[\left(m^2 + \frac{(k_2^b a)^2}{1-\nu}\right)I_m(k_2^b a) - (k_2^b a)I'_m(k_2^b a)\right]. \tag{B.7}$$

$$\beta_{11} = -i^m(k_1 a)J'_m(k_1 a), \quad \beta_{21} = -mi^{m+1}(k_1 a)J_m(k_1 a),$$

$$\beta_{51} = -i^m\left[\left(m^2 - \frac{(k_1 a)^2}{1-\nu}\right)J_m(k_1 a) - (k_1 a)J'_m(k_1 a)\right],$$

$$\beta_{61} = -mi^{m+1}[(k_1 a)J'_m(k_1 a) - J_m(k_1 a)]. \tag{B.8}$$

References

[1] B. Helifa, A. Oulhadj, A. Benbelghit, I. Lefkaier, F. Boubenider, D. Boutassouna, Detection and measurement of surface cracks in ferromagnetic materials using eddy current testing, NDT E Int. 39 (5) (2006) 384–390.

[2] O. Büyüköztürk, Imaging of concrete structures, NDT E Int. 31 (4) (1998) 233–243.

[3] V. Giurgiutiu, Structural Health Monitoring of Aerospace Composites, Academic Press, Oxford, 2015.

[4] S. Banerjee, F. Ricci, E. Monaco, A. Mal, A wave propagation and vibration-based approach for damage identification in structural components, J. Sound Vib. 322 (1–2) (2009) 167–183.

[5] R. Gangadharan, D.R. Mahapatra, S. Gopalakrishnan, C. Murthy, M. Bhat, On the sensitivity of elastic waves due to structural damages: Time–frequency based indexing method, J. Sound Vib. 320 (4–5) (2009) 915–941.

[6] D. Aggelis, T. Matikas, Effect of plate wave dispersion on the acoustic emission parameters in metals, Comput. Struct. 98 (2012) 17–22.

[7] R.J. Barthorpe, On Model-And Data-Based Approaches to Structural Health Monitoring, (Ph.D. thesis), University of Sheffield, 2010.

[8] A.J. Hughes, R.J. Barthorpe, N. Dervilis, C.R. Farrar, K. Worden, A probabilistic risk-based decision framework for structural health monitoring, Mech. Syst. Signal Process. 150 (2021) 107339.

[9] P. Seventekidis, D. Giagopoulos, A. Arailopoulos, O. Markogiannaki, Structural health monitoring using deep learning with optimal finite element model generated data, Mech. Syst. Signal Process. 145 (2020) 106972.

[10] A. Deraemaeker, E. Reynders, G. De Roeck, J. Kullaa, Vibration-based structural health monitoring using output-only measurements under changing environment, Mech. Syst. Signal Process. 22 (1) (2008) 34–56.

[11] C. Farrar, K. Worden, Structural Health Monitoring: A Machine Learning Perspective, John Wiley and Sons, 2012.

[12] H. Fukunaga, N. Hu, F.-K. Chang, Structural damage identification using piezoelectric sensors, Int. J. Solids Struct. 39 (2) (2002) 393–418.

[13] S. Cantero-Chinchilla, G. Aranguren, J.M. Royo, M. Chiachío, J. Etxaniz, A. Calvo-Echenique, Structural health monitoring using ultrasonic guided-waves and the degree of health index, Sensors 21 (3) (2021) 993.

[14] S. He, C.-T. Ng, Guided wave-based identification of multiple cracks in beams using a Bayesian approach, Mech. Syst. Signal Process. 84 (2017) 324–345.

[15] S. Cantero-Chinchilla, J. Chiachío, M. Chiachío, D. Chronopoulos, A. Jones, A robust Bayesian methodology for damage localization in plate-like structures using ultrasonic guided-waves, Mech. Syst. Signal Process. 122 (2019) 192–205.

[16] J. Chiachío, N. Bochud, M. Chiachío, S. Cantero, G. Rus, A multilevel Bayesian method for ultrasound-based damage identification in composite laminates, Mech. Syst. Signal Process. 88 (2017) 462–477.

[17] C. Fendzi, N. Mechbal, M. Rebillat, M. Guskov, G. Coffignal, A general Bayesian framework for ellipse-based and hyperbola-based damage localization in anisotropic composite plates, J. Intell. Mater. Syst. Struct. 27 (3) (2016) 350–374.

[18] Y. Huang, C. Shao, B. Wu, J.L. Beck, H. Li, State-of-the-art review on Bayesian inference in structural system identification and damage assessment, Adv. Struct. Eng. 22 (6) (2019) 1329–1351.

[19] S. Cantero-Chinchilla, M.K. Malik, D. Chronopoulos, J. Chiachío, BayesIan damage localization and identification based on a transient wave propagation model for composite beam structures, Compos. Struct. 267 (2021) 113849.

[20] M. Chiachío, J.L. Beck, J. Chiachio, G. Rus, Approximate Bayesian computation by subset simulation, SIAM J. Sci. Comput. 36 (3) (2014) A1339–A1358.

[21] W.-J. Yan, D. Chronopoulos, C. Papadimitriou, S. Cantero-Chinchilla, G.-S. Zhu, BayesIan inference for damage identification based on analytical probabilistic model of scattering coefficient estimators and ultrafast wave scattering simulation scheme, J. Sound Vib. 468 (2020) 115083.

[22] S.N. Lophaven, H.B. Nielsen, J. Søndergaard, et al., DACE: a Matlab Kriging Toolbox, Vol. 2, Citeseer, 2002.

[23] J.P. Kleijnen, Kriging metamodeling in simulation: A review, European J. Oper. Res. 192 (3) (2009) 707–716.

[24] P. Belanger, P. Cawley, F. Simonetti, Guided wave diffraction tomography within the born approximation, IEEE Trans. Ultrason. Ferroelectr. Freq. Control 57 (6) (2010) 1405–1418.

[25] P. Huthwaite, F. Simonetti, High-resolution guided wave tomography, Wave Motion 50 (5) (2013) 979–993.

[26] J. Rao, M. Ratassepp, Z. Fan, Guided wave tomography based on full wave-form inversion, IEEE Trans. Ultrason. Ferroelectr. Freq. Control 63 (5) (2016) 737–745.

[27] J. Rao, M. Ratassepp, Z. Fan, Investigation of the reconstruction accuracy of guided wave tomography using full waveform inversion, J. Sound Vib. 400 (2017) 317–328.

[28] R. Soleimanpour, C.-T. Ng, Scattering analysis of nonlinear lamb waves at de-laminations in composite laminates, J. Vib. Control (2021) 1077546321990145.

[29] D. Chronopoulos, Calculation of guided wave interaction with nonlinearities and generation of harmonics in composite structures through a wave finite element method, Compos. Struct. 186 (2018) 375–384.

[30] P.D. Wilcox, A. Velichko, Efficient frequency-domain finite element modeling of two-dimensional elastodynamic scattering, J. Acoust. Soc. Am. 127 (1) (2010) 155–165.

[31] J. Zhang, B.W. Drinkwater, P.D. Wilcox, Defect characterization using an ultra-sonic array to measure the scattering coefficient matrix, IEEE Trans. Ultrason. Ferroelectr. Freq. Control 55 (10) (2008) 2254–2265.

[32] A. Velichko, P.D. Wilcox, A generalized approach for efficient finite element modeling of elastodynamic scattering in two and three dimensions, J. Acoust. Soc. Am. 128 (3) (2010) 1004–1014.

[33] M.K. Malik, D. Chronopoulos, G. Tanner, Transient ultrasonic guided wave simulation in layered composite structures using a hybrid wave and finite element scheme, Compos. Struct. 246 (2020) 112376.

[34] X. Cao, L. Zeng, J. Lin, Scattering of lamb waves near lamé point at an opening crack, J. Vib. Acoust. 143 (4) (2021) 041007.

[35] C. Vemula, A. Norris, Flexural wave propagation and scattering on thin plates using Mindlin theory, Wave Motion 26 (1) (1997) 1–12.

[36] A. Norris, C. Vemula, Scattering of flexural waves on thin plates, J. Sound Vib. 181 (1) (1995) 115–125.

[37] J. McKeon, M. Hinders, Lamb wave scattering from a through hole, J. Sound Vib. 224 (5) (1999) 843–862.

[38] L. Moreau, M. Caleap, A. Velichko, P. Wilcox, Scattering of guided waves by flat-bottomed cavities with irregular shapes, Wave Motion 49 (2) (2012) 375–387.

[39] L. Moreau, M. Caleap, A. Velichko, P. Wilcox, Scattering of guided waves by through-thickness cavities with irregular shapes, Wave Motion 48 (7) (2011) 586–602.

[40] T. Grahn, Lamb wave scattering from a circular partly through-thickness hole in a plate, Wave Motion 37 (1) (2003) 63–80.

[41] O. Diligent, T. Grahn, A. Boström, P. Cawley, M.J. Lowe, The low-frequency reflection and scattering of the S 0 Lamb mode from a circular through-thickness hole in a plate: Finite element, analytical and experimental studies, J. Acoust. Soc. Am. 112 (6) (2002) 2589–2601.

[42] S.H. Díaz Valdés, C. Soutis, Real-time nondestructive evaluation of fiber com-posite laminates using low-frequency lamb waves, J. Acoust. Soc. Am. 111 (5) (2002) 2026–2033.

[43] D.N. Alleyne, P. Cawley, Optimization of Lamb wave inspection techniques, NDT E Int. 25 (1) (1992) 11–22.

[44] A. Huber, Dispersion Calculator User's Manual, German Aerospace Center (DLR), Augsburg, Germany, 2019.

[45] O. Diligent, T. Grahn, A. Boström, P. Cawley, M.J. Lowe, The low-frequency reflection and scattering of the S 0 Lamb mode from a circular through-thickness hole in a plate: Finite element, analytical and experimental studies, J. Acoust. Soc. Am. 112 (6) (2002) 2589–2601.

[46] A. Demma, P. Cawley, M. Lowe, A. Roosenbrand, The reflection of the funda-mental torsional mode from cracks and notches in pipes, J. Acoust. Soc. Am. 114 (2) (2003) 611–625.

[47] J. Chiachio-Ruano, M. Chiachio-Ruano, S. Sankararaman, Bayesian Inverse Problems: Fundamentals and Engineering Applications, CRC Press, 2021.

[48] J.L. Beck, BayesIan system identification based on probability logic, Struct. Control Health Monit. 17 (7) (2010) 825–847.

[49] E.T. Jaynes, Information theory and statistical mechanics, Phys. Rev. 106 (4) (1957) 620.

[50] R.M. Neal, Probabilistic Inference using Markov Chain Monte Carlo Methods, Department of Computer Science, University of Toronto Toronto, ON, Canada, 1993.

[51] N. Metropolis, A.W. Rosenbluth, M.N. Rosenbluth, A.H. Teller, E. Teller, Equation of state calculations by fast computing machines, J. Chem. Phys. 21 (6) (1953) 1087–1092.

[52] W.K. Hastings, Monte Carlo Sampling Methods Using Markov Chains and Their Applications, Oxford University Press, 1970.

[53] ABAQUS, Abaqus Documentation, Dassault Systèmes, Providence, RI, USA, 2016.

[54] Z. Su, L. Ye, Identification of Damage using Lamb Waves: From Fundamentals to Applications, Vol. 48, Springer Science & Business Media, 2009.

[55] Z. Su, L. Ye, Selective generation of lamb wave modes and their propagation characteristics in defective composite laminates, Proc. Inst. Mech. Eng. L J. Mater. Des. Appl. 218 (2) (2004) 95–110.

[56] V. Giurgiutiu, Tuned lamb wave excitation and detection with piezoelectric wafer active sensors for structural health monitoring, J. Intell. Mater. Syst. Struct. 16 (4) (2005) 291–305.

[57] S. Grondel, C. Paget, C. Delebarre, J. Assaad, K. Levin, Design of optimal config-uration for generating A 0 lamb mode in a composite plate using piezoceramic transducers, J. Acoust. Soc. Am. 112 (1) (2002) 84–90.

[58] V. Giurgiutiu, Wave tuning with piezoelectric wafer active sensors, in: Struct. Health Monit. Piezoelectric Wafer Act. Sens, 2014, pp. 573–637.

[59] N. Yue, M. Aliabadi, A scalable data-driven approach to temperature baseline reconstruction for guided wave structural health monitoring of anisotropic carbon-fibre-reinforced polymer structures, Struct. Health Monit. 19 (5) (2020) 1487–1506.